IPSJ Transactions on Computer Vision and Applications Vol. 1 288–300 (Dec. 2009)

Technical Note

Estimating Sunlight Polarization Using a Fish-eye Lens

Daisuke Miyazaki,[†1,*1] Mahdi Ammar,[†1,*2]
Rei Kawakami[†1] and Katsushi Ikeuchi[†1]

In outdoor scenes, polarization of the sky provides a significant clue to understanding the environment. The polarized state of light conveys the information for obtaining the orientation of the sun. Robot navigation, sensor planning, and many other application areas benefit from using this navigation mechanism. Unlike previous investigations, we analyze sky polarization patterns when the fish-eye lens is not vertical, since a camera in a general position is effective in analyzing outdoor measurements. We have tilted the measurement system based on a fish-eye lens, a CCD camera, and a linear polarizer, in order to analyze transition of the 180-degree sky polarization patterns while tilting. We also compared our results measured under overcast skies with the corresponding celestial polarization patterns calculated using the single-scattering Rayleigh model.

1. Introduction

The polarization pattern of the sky conveys rich information about the orientation of the sun. Voyagers and polarization-sensitive animals use sky polarization patterns as a compass. Many theoretical and experimental studies [1),2)] have been done because the understanding of these optical characteristics has been one of the most interesting and important problems in atmospheric optics. In this paper, we first show our results of sky polarization patterns obtained by a camera with a fish-eye lens in order to affirm that the theoretical and experimental studies [1)–3)] are trustworthy. In addition, unlike the previous studies, we tilt the fish-eye lens camera and analyze the sky polarization patterns of this as-yet-uninvestigated situation.

In Section 2, we will briefly review the fundamental theory of sky polarization. Section 3 describes our original work that analyzes the sky polarization pattern when the camera is tilted. We show some measurement results in Section 4, and present a discussion in Section 5.

†1 Institute of Industrial Science, The University of Tokyo
∗1 Presently with Hiroshima City University
∗2 Presently with Ecole Supérieure de Physique et de Chimie Industrielles

2. Materials and Methods

2.1 Measurement of the Celestial Polarization Pattern Using Sky Imaging Polarimetry

Our polarimetric measurements were performed at The University of Tokyo, Institute of Industrial Science (35°40′ N, 139°40′ E), on different dates in June and July 2008, one or two hours before sunset. The setup of our full-sky imaging polarimetry is shown in **Fig. 1**. The technique used here was similar to the technique described in the latest publications [1)–3),5)]. The detector was a digital sensor of a DSLR (digital single-lens reflex) camera (Canon EOS 5D): The maxima and half-bandwidths of its spectral sensitivity curves were: Red = 620 ± 50 nm, green = 530 ± 30 nm, and blue = 470 ± 30 nm. The fish-eye lens (Sigma EX

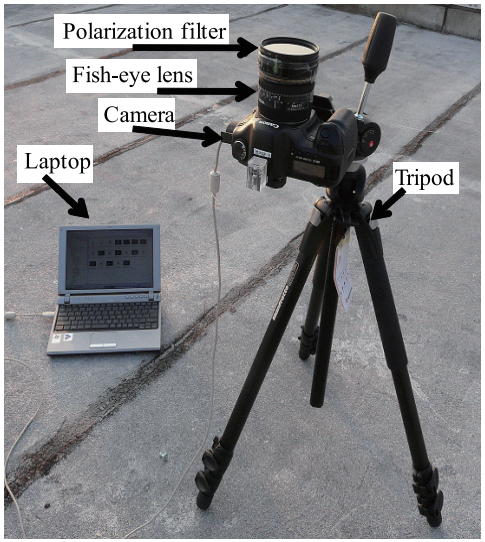

Fig. 1 Imaging polarimetry system (linear polarizer, fish-eye lens, Canon camera, tripod, and a laptop).

DG fish-eye, F = 3.5, focal length 8 mm) ensured an angle of view of 180°. The polarizing filter (Kenko PL, 72 mm) enabled the measurement of the sky polarization patterns. However, using a commercial DSLR camera, it was imperative to set up the polarizing filter in front of the fish-eye lens. Hence, our imaging polarimeter allowed only an angle of view of 130°. Using a personal computer and Canon software (EOS utility), three photographs were taken for three different alignments of the transmission axis of the polarizer (0, 45°, and 90° clockwise from the top view of the camera). The polarizer was rotated manually. The initial position of the camera was set up on a tripod such that its axis passing through the view-finder pointed northwards and the optical axis of the fish-eye lens was vertical.

Using a personal computer, we converted the raw images linearly to 16-bit uncompressed TIFF images. The patterns of the degree and angle of polarization of sky light were determined and visualized as high-resolution, color-coded, two-dimensional circular maps. Each map contained approximately 3,140,000 pixels. These patterns were obtained in the red, green, and blue spectral ranges. The three-dimensional celestial hemisphere was represented in two dimensions by a polar-coordinate system, where the zenith angle θ and the azimuth angle φ from the camera top view axis (x-axis) were measured radially and tangentially, respectively (**Fig. 2**). In this two-dimensional coordinate system, the zenith was at the origin and 65° of the zenith-axis corresponded to the outermost circle.

Our imaging polarimeter was calibrated as follows: During evaluation of the recordings to obtain the intensity of the sky light, and the degree and angle of polarization of the sky light, the following characteristics were taken into consideration: (i) The measured Mueller matrix of the fish-eye lens as a function of the angle of incidence with respect to the optical axis; (ii) The angular distortion of the fish-eye lens, i.e., the measured angular distance from the zenith versus the angle of incidence (the off-axis angle); ideally, they are equal (Fig. 2 (c)); (iii) The decrease in light intensity imaged on the sensor because of the decrease in the effective aperture with increasing angle of incidence (roll-off calibration); and (iv) The transmission of the polarizing filter as a function of the wavelength. Characteristics (i–iv) describe how the angular imaging, intensity, polarization, and spectral composition of the incident light are influenced by the optics and

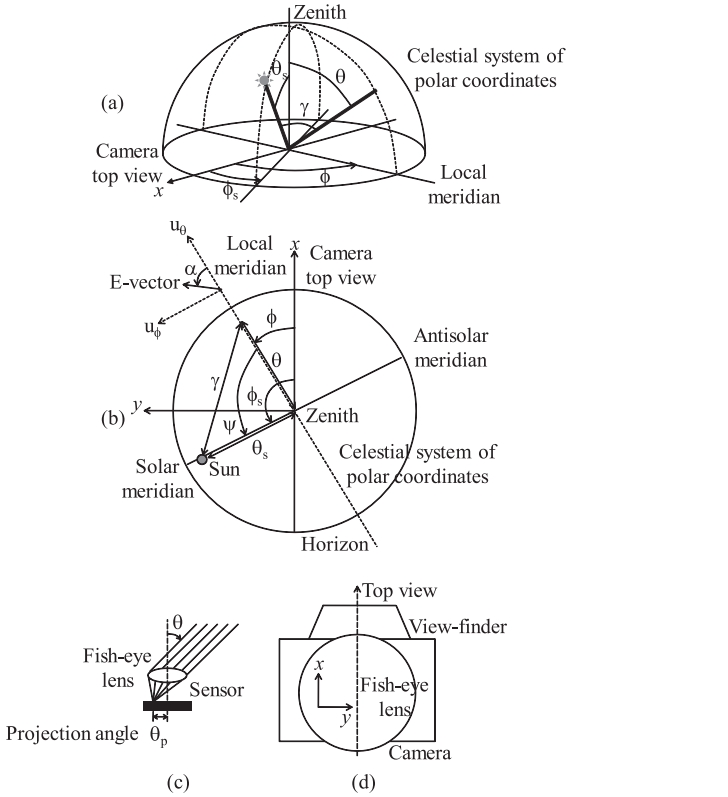

Fig. 2 Three- (a) and two-dimensional (b) representation of the celestial polar coordinates system used in the representation of the sky polarization patterns. (c) Schematic representation of the relationship between the off-axis angle θ and the projection angle θ_p projected onto the digital sensor by the fish-eye lens. Ideally: $\theta_p = \theta$. (d) Schematic representation of the camera: a clockwise angle from the top view of the camera becomes a counterclockwise angle on the photo. (Redrawn, in part, from Ref. 3))

detector of the polarimeter system (Section 4.1 [3),4)]).

2.2 Polarization Calculations Using the Single-scattering Rayleigh Model

Light radiated by the sun is unpolarized; however, on its way through the earth's atmosphere, sunlight is scattered by air molecules, i.e., by particles much

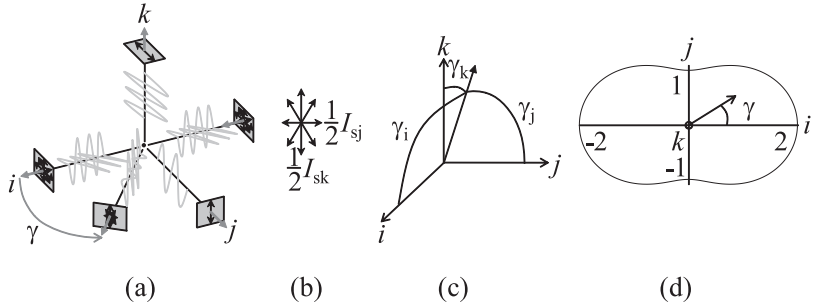

Fig. 3 (a) Polarization arising from light scattering within the earth's atmosphere. Unpolarized sunlight remains unpolarized if the scattering angle is 0°. The degree of polarization reaches 100% if the scattering angle is 90°. Other scattering angles yield smaller degrees of polarization. (b) j and k axes of partially polarized light. (c) The definition of the angles γ_i, γ_j, and γ_k. (d) Shape of the scattering intensity as a function of scattering angle for scattering of a small particle. (Redrawn, in part, from Ref. 13))

smaller than the wavelength. The light scattering intensity depends on the scattering angle and the wavelength such that [12]:

$$I(\gamma) = \frac{K}{\lambda^4}\left(1 + \cos^2\gamma\right), \tag{1}$$

where K is a constant of proportionality, λ is the wavelength, and γ is the angular distance between the observed celestial point and the sun. The shape of the intensity diagram is determined by the $(1 + \cos^2\gamma)$ term. A plot of this term is given in **Fig. 3** (d). Since the sun is quite far from the earth, it can be assumed as a directional light. Therefore, we denote both the scattering angle and the angle between the molecule direction and the sun direction with the same variable, γ (**Fig. 4**).

Sunlight remains unpolarized if it reaches the observer directly (scattering angle 0°), but is linearly polarized if it is scattered by molecules within the atmosphere. Within a theoretical (Rayleigh) atmosphere, the degree of polarization reaches 100% if the scattering angle is 90°. Other scattering angles yield smaller degrees of polarization. The light is then said to be partially linearly polarized (Fig. 3).

This scattering results in the polarization of light: the E-vector is oriented perpendicularly to the plane of scattering formed by the sun, the observed point, and the observer (**Fig. 5** (a)). Here, E-vector means the orientation of the electric

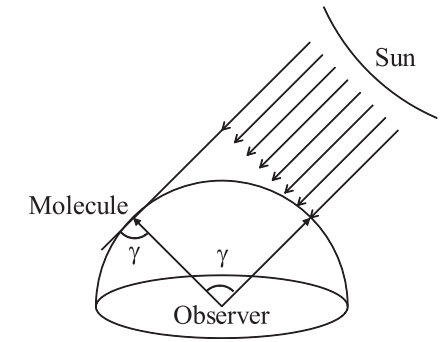

Fig. 4 The definition of the angle γ. Since the sun is quite far from the earth, γ represents not only the scattering angle of the molecule but also the angle between the direction from the observer to the molecule and the direction from the observer to the sun.

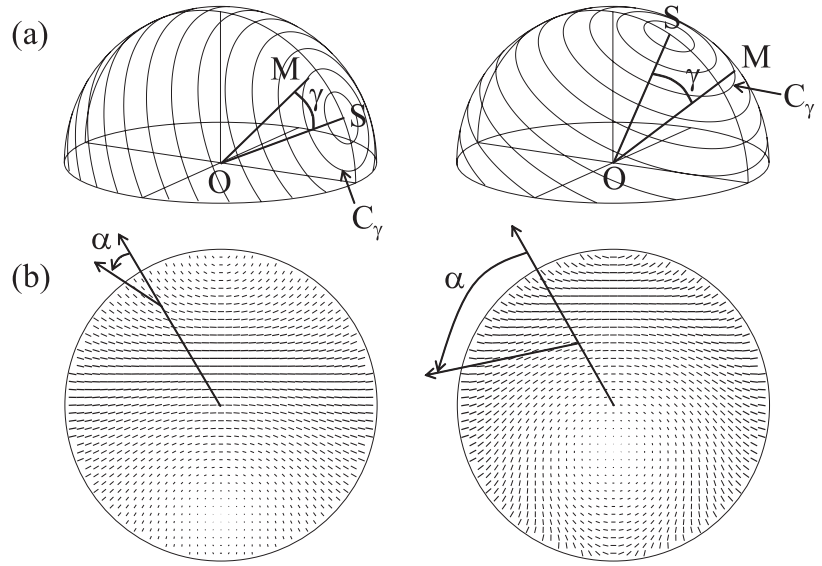

Fig. 5 Three- (a) and two-dimensional (b) representation of the pattern of polarized light in the sky depicted for two different elevations of the sun (left: $\theta_s = 65°$, right: $\theta_s = 25°$). In (b), the orientation and the size of the black mark represent the direction (α) and the degree of polarization (d), respectively. (Redrawn, in part, from Ref. 7))

vector of light (i.e., electromagnetic radiation), namely, the orientation of the polarized light. From geometrical consideration, the E-vector orientation from the local meridian, which we denote as α, is expressed as (Appendix A.1.2):

$$\tan\alpha = \frac{\cos\theta\sin\theta_s\cos\psi - \sin\theta\cos\theta_s}{\sin\theta\sin\theta_s\sin\psi}, \tag{2}$$

where θ_s is the solar zenith angle, and θ and ψ are the angular distances of the observed point from the zenith and the solar meridian, respectively (Fig. 5 (a)).

Figure 5 reveals a sky light phenomenon, depicted by the size of the black lines. Apart from the orientation α of the E-vector, it is also the degree of polarization d that varies across the celestial hemisphere. According to the Rayleigh theory, d depends on the scattering angle γ such that (Appendix A.1.1):

$$d = \frac{\sin^2\gamma}{1+\cos^2\gamma}. \tag{3}$$

d varies from 0 ($\gamma = 0°$, direct unscattered and hence unpolarized light) to 1 or 100% ($\gamma = 90°$, great circle of maximally polarized light extending across the sky at an angular distance of 90° from the sun). The degree of polarization d does not depend on the red, green, or blue channels of the camera, as is discussed in Appendix A.1.1.

2.3 Data Processing and Analysis

In order to analyze the sky light patterns, we calculated the intensity I, degree of polarization d, and E-vector orientation α. This polarization analysis was based on Stokes parameters for partially polarized light [11]. It is worth noticing that the light in the atmosphere is not circularly polarized [9], so we do not need to evaluate this quantity (i.e., we assume that the light in the atmosphere is partially linearly polarized).

In short, if I_0, I_{45}, and I_{90} represent the intensity values recorded when the polarizing filter is at 0°, 45°, and 90° from the camera top view, respectively, then, from geometrical considerations, the orientation of polarization α' (representing the E-vector shift from the top view) is given by:

$$\alpha' = \frac{1}{2}\arctan\left(\frac{I_0 + I_{90} - 2I_{45}}{I_{90} - I_0}\right). \tag{4}$$

We used the following α'' which is scaled between $-90°$ and 90°.

$$\alpha'' = \begin{cases} \alpha' & (I_{90} < I_0) \\ \alpha' + 90° & (I_{90} \geq I_0) \wedge (I_{90} + I_0 < 2I_{45}) \\ \alpha' - 90° & (I_{90} \geq I_0) \wedge (I_{90} + I_0 \geq 2I_{45}) \end{cases}. \tag{5}$$

Finally, α was expressed as an angle drifted from the local meridian, in order to analyze the E-vector orientation patterns independently of the initial position of the polarizer such that (Fig. 2):

$$\alpha = \alpha'' - \varphi. \tag{6}$$

Again, α'' is the E-vector orientation, φ is the local meridian, and α is the E-vector orientation from the local meridian (Appendix A.1.2, Figs. 2 and 5). The total intensity was given by:

$$I = I_0 + I_{90}, \tag{7}$$

while the degree of polarization was given by:

$$d = \frac{\sqrt{(I_0 + I_{90})^2 + (I_0 + I_{90} - 2I_{45})^2}}{I_0 + I_{90}}. \tag{8}$$

2.4 Neutral Points

Rayleigh's explanation of the polarization of clear sky would predict that light is unpolarized in the direction of the sun or anti-sun (= opposite of the sun), whichever is above the horizon. But observations had already demonstrated the existence of three unpolarized directions: above the sun (the Babinet point), below the sun (the Brewster point), and above the anti-sun (the Arago point), and hinted at a fourth point below the anti-sun (**Fig. 6**). The deviation from the sun and anti-sun is interpreted as a multiple-scattering effect, which splits the unpolarized points of the single-scattering theory into two points; this phenomenon has been considerably elaborated [8]. These unpolarized points typically lie within 15–35° of the sun or anti-sun.

In the red, green, and blue spectral ranges, the zenith distances of the Arago and Babinet neutral points were determined by a simple method, which took into consideration that (i) the sky light was unpolarized ($d \sim 0\%$) in a neutral point; (ii) the degree of polarization gradually increased with increasing angular distance from the neutral point; and (iii) the sky light polarization switched from negative to positive (that is, the angle of polarization α suffered a change of $\Delta\alpha = 90°$

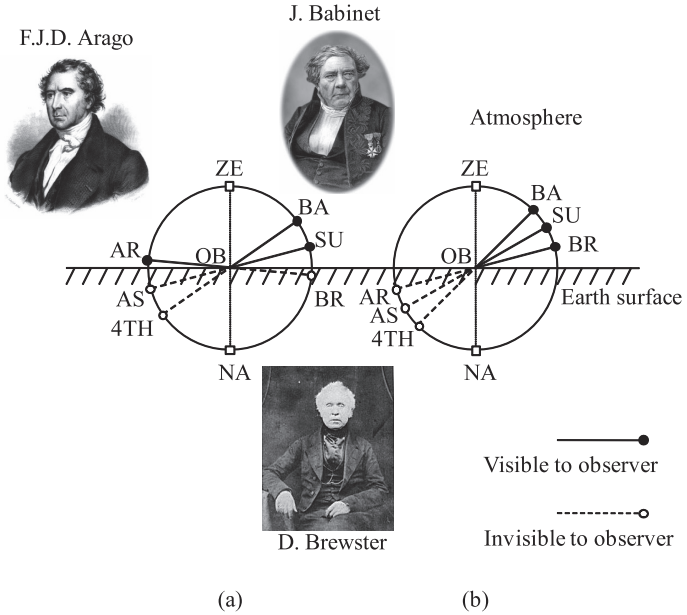

Fig. 6 Schematic diagram showing the normal positions of the Arago (AR), Babinet (BA), and Brewster (BR) neutral points of sky light polarization in the vertical plane including the ground-level observer (OB), sun (SU), zenith (ZE), anti-solar point (AS), and nadir (NA). From the ground, only two neutral points are visible simultaneously: Either the Arago and Babinet points ((a), for lower solar elevations), or the Babinet and Brewster points ((b), for higher solar elevations). (Redrawn from Ref. 5))

as one passed a neutral point). The points possessing these characteristics were recognized in a given sky. Then, the position of the Arago or Babinet point was obtained as the geometric center (center of mass) of these points.

3. Polarization Measurements Using a Camera in General Position

The contribution of this paper is to analyze the sky polarization patterns when the camera is tilted from the horizon. All the recent studies of sky polarization patterns [1)–3)] were performed using a camera sensor set up in the horizontal plane (i.e., the optical axis of the fish-eye lens was vertical to the ground). This condition is considered as a serious limitation if we try to apply the latest method in the field of computer vision. We are interested not only in the sky light patterns but

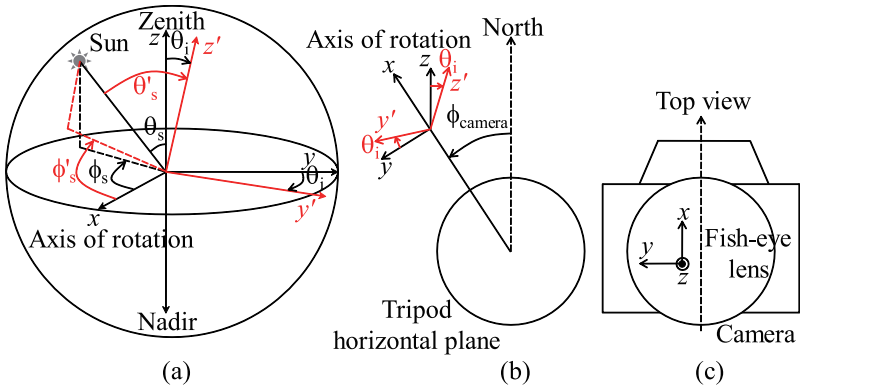

Fig. 7 (a) The sun coordinates in the camera reference (x, y, z) while the optical axis of the fish-eye lens is the z-axis, and after rotation of the camera around the x-axis in the reference (x, y', z'). (b) The camera orientation from the north. (c) Schematic representation of the camera and the camera reference (x, y, z).

also in the object's appearance (reflectance) in the outdoor environment. Therefore, it is worth trying to analyze simultaneously both light and object. When we take a photo in the outdoors, only a small part of the sky is visible, and the camera sensor is not horizontal. Hence, it is worth investigating sky polarization patterns using a camera in a general position (i.e., the optical axis of the fish-eye lens is not necessarily vertical). Using a tripod, it is possible to rotate the camera top-view (x-axis) from the north (φ_{camera}), and to rotate the optical axis of the fish-eye lens (z-axis) around the x-axis of the camera reference (x, y, z).

To simulate sky polarization patterns using the Rayleigh single-scattering model (Eq. (2)), the coordinates of the sun (θ'_s, φ'_s) in the new camera reference (x, y', z') are the only required parameters: $\mathbf{OS}' = R(x, \theta_i) \cdot \mathbf{OS}$, where $R(x, \theta_i)$ is the rotation matrix around x-axis by angle θ_i, and $\mathbf{OS}$ and $\mathbf{OS}'$ are the sun coordinate vectors in (x, y, z) and (x, y', z'), respectively (**Fig. 7**).

In detail:

$$\begin{bmatrix} \sin\theta'_s \cos\varphi'_s \\ \sin\theta'_s \sin\varphi'_s \\ \cos\theta'_s \end{bmatrix} = \begin{bmatrix} 1 & 0 & 0 \\ 0 & \cos\theta_i & -\sin\theta_i \\ 0 & \sin\theta_i & \cos\theta_i \end{bmatrix} \begin{bmatrix} \sin\theta_s \cos\varphi_s \\ \sin\theta_s \sin\varphi_s \\ \cos\theta_s \end{bmatrix}. \quad (9)$$

Therefore, the sun coordinates (θ_s, φ_s) in the horizontal plane could be determined from (θ'_s, φ'_s) by the following equations:

$$\begin{cases} \sin\theta_s \cos\varphi_s = \sin\theta'_s \cos\varphi'_s & \text{(I)} \\ \sin\theta_s \sin\varphi_s = \cos\theta_i \sin\theta'_s \sin\varphi'_s + \sin\theta_i \cos\theta'_s & \text{(II)} \\ \cos\theta_s = -\sin\theta_i \sin\theta'_s \cos\varphi'_s + \cos\theta_i \cos\theta'_s & \text{(III)} \end{cases} . \quad (10)$$

4. Results

4.1 Imaging Polarimetry Calibration

Our 180° field-of-view fish-eye lens formed a circular image with a radius of R = 1,400 pixels in its focal plane (on the digital sensor) from the object field. The incident rays originating from a given off-axis angle θ were focused into a given point of this circular image at a distance r from the center. The value of the so-called "projection angle" was calculated as $\theta_p = 90°r/R$. In order to determine the relationship between θ and θ_p, we rotated the camera with a frequency of 5° around the x-axis, and we took pictures of a point source located far away from the camera (Fig. 2 (c)). As shown in **Fig. 8** (a), the relationship between θ and θ_p was very close to the ideal case: $\theta = \theta_p$. The roll-off problem (the decrease in the effective aperture with increasing angle of incidence) was also insignificant, as shown in Fig. 8 (b).

In order to determine the change of optical properties of the light passing through the fish-eye lens (without polarizing filter), we had to know its system Mueller matrix as a function of the off-axis angle θ. In general, this means that we have to know the function of all its 16 elements. However, in the case of our full-sky imaging polarimeter, we did not need all of these elements. The reasoning behind this is as follows:

(1) Since the digital sensor was sensitive only to the intensity of the incoming light, only the first row $(M_{11}, M_{12}, M_{13}, M_{14})$ of the total Mueller matrix needed to be determined.

(2) In general, the light in the atmosphere is not circularly polarized, and so we did not need to measure M_{14}.

(3) According to the standard calibration methods [3], we used the reduced Mueller matrix $\mathbf{m}$, which is the system Mueller matrix normalized to M_{11} $(m_{ij} = M_{ij}/M_{11})$.

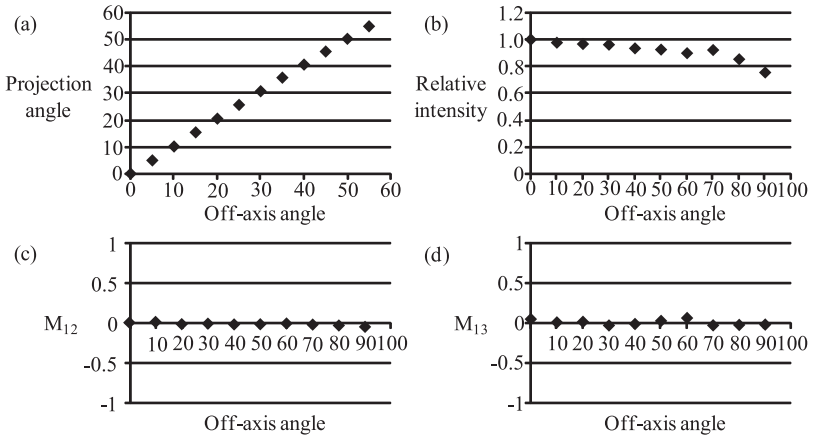

Fig. 8 Optical characteristics of the imaging polarimeter: (a) the angular distortion of the fish-eye lens: The projection angle versus the angle of incidence (ideally they are equal); (b) the decrease in light intensity imaged on the sensor because of the decrease in the effective aperture with increasing angle of incidence (roll-off calibration); (c–d) the measured Mueller matrix of the fish-eye lens as a function of the angle of incidence with respect to the optical axis.

Consequently, it was enough to determine $m_{12}(\theta)$ and $m_{13}(\theta)$. As shown in Fig. 8 (c–d), $m_{12}(\theta)$ and $m_{13}(\theta)$ were almost equal to zero, which meant that the light polarization patterns were unchanged after passing through the fish-eye lens.

Using a spectrophotometer, the transmission of the polarizing filter as a function of the wavelength was determined by calculating the ratio between the light intensities measured with and without the polarizing filter. As shown in **Fig. 9**, the transmission of the polarizing filter was almost independent of the wavelength in the spectral range 400–700 [nm], contrarily to the camera sensor, which is more sensitive in the green than the red and the blue spectral ranges.

4.2 Polarization Sky Patterns

We measured the patterns of the degree of linear polarization d, and the angle of polarization α of a clear sky by our sky-imaging polarimetry in the red 650 nm, green 550 nm, and blue 450 nm parts of the spectrum.

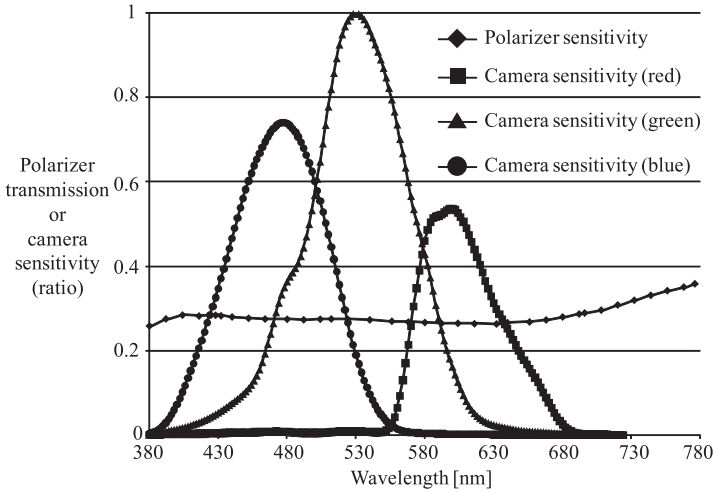

Fig. 9 The transmission of the polarizing filter and the camera sensor sensitivity as a function of the wavelength.

As expected, d from the clear sky was highest at 90° from the sun and gradually decreased toward the solar and antisolar points (**Fig. 10** (a)). Furthermore, d was highest in the red ($d_{\max} = 65\%$) and lowest in the blue ($d_{\max} = 39\%$) part of the spectrum (**Table 1**).

The angle of polarization of light from the clear sky had a characteristic pattern (Fig. 10 (a)): The isolines with constant were always shaped like an eight with a center at the zenith and an axis of mirror symmetry coinciding with the solar-antisolar meridian in such a way that the smaller loop of the eight was always in the solar half of the sky.

Like Pomozi, et al. [2], we also calculated the theoretical sky polarization in order to evaluate the measured data scientifically. Comparison of the measured (Fig. 10 (a)) and theoretical (Fig. 10 (d)) patterns indicated that, apart from regions near the sun and anti-sun, the simple single-scattering Rayleigh theory described the characteristics of the sky polarization patterns relatively well. The most striking differences between the actual and the theoretical patterns were the consequences of the neutral (unpolarized) points. Because of these neutral points, the isolines belonging to given values of the degree and angle of polarization differed more or less from each other in the real and the Rayleigh sky.

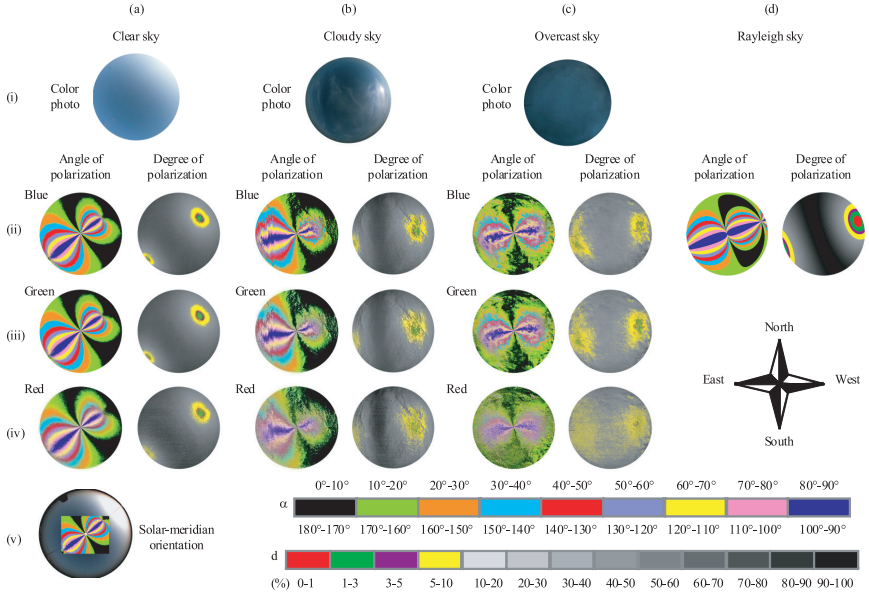

Fig. 10 The double-check experiments of Ref. 2). Color picture (i), degree of linear polarization d (ii–iv, right), and angle of polarization α (ii–iv, left) calculated clockwise from the local meridian were measured by full-sky imaging polarimetry in the red (650 nm), green (550 nm), and blue (450 nm) parts of the spectrum in different sky conditions (clear sky (a), cloudy sky (b), and overcast sky (c)). (d) Patterns of the degree and angle of polarization of sky light calculated using the single-scattering Rayleigh model. The optical axis of the fish-eye lens was vertical and the center of the circular patterns was the zenith.

Table 1 The degree of linear polarization d (average ± standard deviation) is averaged over the entire sky for different sky conditions.

	Degree of linear polarization (%)		
	Clear sky	Cloudy sky	Overcast sky
Blue	32 ± 12	17 ± 6	12 ± 6
Green	31 ± 12	15 ± 5	10 ± 5
Red	34 ± 14	15 ± 7	10 ± 7

Figure 10 (b) and Fig. 10 (c) represent the patterns of the degree and angle of polarization of partially cloudy and overcast skies measured again in the blue,

green, and red spectral ranges. The most outstanding observation was that the angle of polarization of both cloudy and overcast sky were qualitatively the same as those of the clear sky (Fig. 10 (b) and Fig. 10 (c)), which is in accordance with previous results [1].

As shown in Fig. 10 (a-v), the neutral line expresses the sun orientation (sun azimuth) with excellent precision (less than 3° of error) for a clear sky. For an overcast sky, the sun orientation was determined within 10° of precision.

Nevertheless, the angle of polarization patterns does not give the exact position of the sun (sun elevation). The sun elevation could be approximately determined using an empirical relationship between the neutral points and the sun position ($\theta_s = \theta_{\text{Babinet}} + 30°, \theta_s = \theta_{\text{Arago}} + 20°$, for the blue in clear sky condition [5]).

4.3 Observation under Tilted Camera

Unlike the previous studies, we have performed experiments when the camera is tilted (Section 3). The optical axis of the fish-eye lens was set up at 35° from the vertical (Fig. 7; $\theta_i = -35°$). The camera was rotated progressively 15° counterclockwise from the north (around the z-axis of the tripod, Fig. 7) and the sky polarization patterns were measured twice each time to minimize the errors due to the manual rotation of the polarizing filter. All the measurements were taken in 20 minutes; hence, it is reasonable to assume that the sun and the neutral points were immovable during the measurements (since, in Tokyo, the solar meridian is rotated counterclockwise about 4°/20[min]).

As shown in **Fig. 11**, the angle α and the degree of polarization d present similar patterns with those shown in Fig. 10 (taken while the optical axis of the fish-eye lens was vertical). Although the α-patterns are always eight-shaped, the Arago, the Babinet, and the center of the circular patterns do not form a line anymore. However, the solar meridian orientation could be evaluated from the α-pattern using neutral point (Arago or Babinet) coordinates and Eqs. (10) (I, II, III) presented previously.

It is also worth noticing that the Babinet and Arago neutral points do not obey the rule presented previously. From now on, the Babinet point could be located on the top of the bigger loop (Fig. 11 (b-ii)). Hence, the distinction between the Arago and the Babinet points becomes slightly more complicated but always possible by calculating their coordinates in the horizontal plane using Eqs. (10)

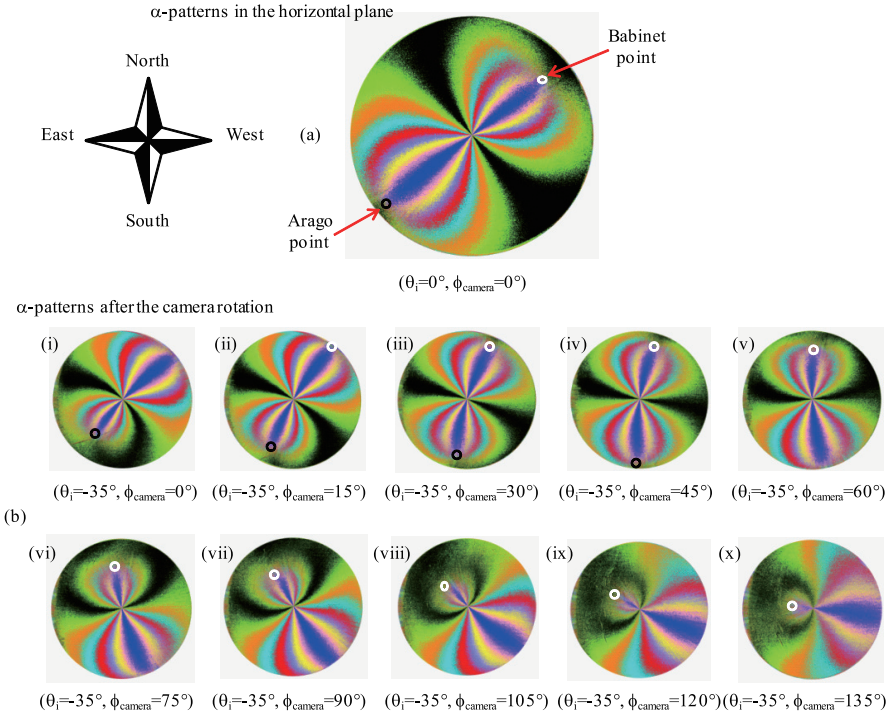

Fig. 11 (a) The angle of polarization patterns of the sky measured while the optical axis of the fish-eye lens was vertical. (b) The angles of polarization patterns of the sky measured after rotation of the optical axis of the fish-eye lens (−35°) from the vertical around the x-axis of the camera, and progressive rotation of the camera from the north by 15° around the vertical (z-axis) of the tripod (Fig. 7). The positions of the Arago and Babinet neutral (unpolarized) points are marked by black and white circles, respectively.

(I, II, III).

Equations (10) (I, II, III) could be used to determine the solar meridian orientation φ_s from the north by measuring the Babinet (or the Arago) coordinates (θ'_b, φ'_b) (since $\varphi_s = \varphi_{\text{Babinet}} = 180° + \varphi_{\text{Arago}}$, and $\theta_s = \theta_{\text{Babinet}} + 30°$ from the end of Section 4.2). To evaluate the accuracy of this method, the Babinet (or the Arago) coordinates (θ'_b, φ'_b) were measured from the images (Fig. 11 (b)) and compared to the Babinet coordinates (θ_b, φ_b) in the horizontal plane measured

from the image (Fig. 11 (a)) by using the following ratios (R_1, R_2, R_3) derived from Eqs. (10) (I, II, III):

$$\begin{cases} R_1 = \dfrac{\sin\theta'_b \cos\varphi'_b}{\sin\theta_b \cos\varphi_b} \\ R_2 = \dfrac{\cos\theta_i \sin\theta'_b \sin\varphi'_b + \sin\theta_i \cos\theta'_b}{\sin\theta_b \sin\varphi_b} \\ R_3 = \dfrac{-\sin\theta_i \sin\theta'_b \sin\varphi'_b + \cos\theta_i \cos\theta'_b}{\cos\theta_b} \end{cases} . \tag{11}$$

These ratios are used only for evaluation, and are not necessary for analyzing the sky polarization. All these ratios should be equal to one if this method was accurate. We found Eqs. (10) (I and III) are accurate; however, Eq. (10) (II) seems to be unstable and very sensitive to errors of measurements (**Fig. 12**). The reason for this instability might be that Eq. (10) (II) is certainly the most complex, requiring all the parameters. In addition, Eq. (10) (II) represents the y-axis, which will be zero when the camera is rotated 90°.

Fortunately, the problem could be solved using only two Eqs. (10) (I, III). Therefore, the solar meridian orientation could be evaluated accurately using the Babinet or the Arago neutral point coordinates and Eqs. (10) (I, III). Finally, the exact sun position could be determined using the method described previously (Section 4.2).

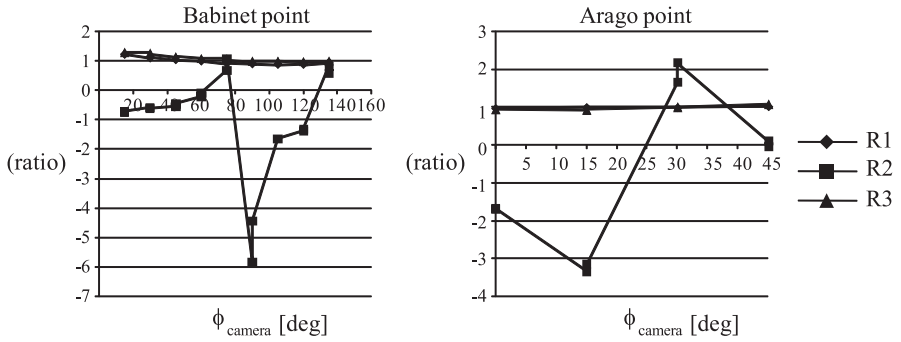

Fig. 12 The accuracy of the determination of the solar meridian orientation using the Babinet and Arago neutral points and Eqs. (10) (I, II, III). The ratios Eq. (11) R_1, R_2 and R_3 were calculated using the measurements of the Babinet and the Arago coordinates from the images (Fig. 11). Those ratios should be equal to one if Eqs. (10) (I, II, III) were accurate.

5. Discussion

5.1 Polarization Sky Patterns

First, we set the fish-eye lens vertically to the ground. We measured the sky polarization pattern under this setup, in order to examine whether or not our setup could capture the same pattern as the previous results.

The sky polarization pattern was examined using the degree d and angle α of linear polarization, and these values are shown in Fig. 10. We also compared the obtained data with the Rayleigh model in order to analyze the performance of our setup. As is shown by Pomozi, et al. [2], our results also showed that the sky polarization pattern of the clear sky (Fig. 10 (a)) followed almost the same pattern of the Rayleigh model (Fig. 10 (d)). The Rayleigh model only assumes a single scattering, while the real sky causes multiple scattering. Due to its multiple scattering, we observed the neutral points, where the degree of polarization was zero, around the sun and the anti-sun.

The degree of polarization under a cloudy sky (Fig. 10 (b)) and an overcast sky (Fig. 10 (c)) was less than that under a clear sky (Fig. 10 (a)) due to the multiple scattering through thick clouds. The pattern of d differed greatly from the theory, and thus, it was difficult to detect the sun orientation from it. On the other hand, the degree of polarization detected the weather (clear, cloudy, overcast, foggy, and hazy skies).

The angle of polarization under a cloudy sky (Fig. 10 (b)) and an overcast sky (Fig. 10 (c)) showed almost the same pattern as that under a clear sky (Fig. 10 (a)). As is shown in previous investigations, we also obtained the eight-shaped pattern of α. The pattern was symmetrical along the solar-antisolar meridian. These results showed that even if the sun was occulted by thick clouds, we could estimate the orientation of the sun. This robustness of estimation encourages us to further use sky polarization in the field of computer vision.

5.2 Observation under Tilted Camera

In this paper, we have presented the results of our investigation of polarization sky patterns when the camera is tilted. We have presented an accurate method to determine the solar meridian orientation from photos taken outdoors, using a

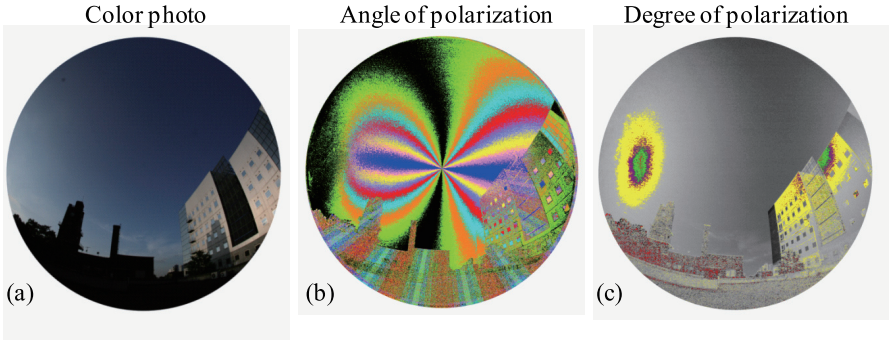

Fig. 13 (a) Color photo of an outdoor scene (Institute of Industrial Science, The University of Tokyo), (b) angle of polarization pattern: The smaller loop of the eight-shape appears roughly on the solar meridian direction in the photo, (c) degree of polarization pattern.

polarizing filter, while only a small part of the sky is available and the camera sensor is not horizontal.

For instance in **Fig. 13**, the solar meridian orientation could be determined from photos of an outdoor scene using the angle of polarization pattern even if the eight-shape is not complete. Therefore, the orientation of the camera could be determined from the solar meridian. This is of great importance for orientation purposes in computer vision, for example, in determining the sensor orientation for 3D-modeling of outdoor objects.

This method also allows evaluation of the sun orientation in the photo, and so the distinction between sunlight and sky light could be performed unambiguously in an outdoor scene (Fig. 13 (b)). This is of great importance in photometric and image analysis where the localization of the light source is usually a main issue.

Finally, using the degree of polarization patterns (Fig. 13 (c)), the sky condition in the photo (clear, foggy, cloudy, or overcast sky) could be determined precisely, and knowing the sun position (by applying the previous method), the outdoor scene appearance could be simulated under different atmospheric conditions.

Acknowledgments This research was supported in part by the Ministry of Education, Culture, Sports, Science and Technology under the Leading Project, "Development of High Fidelity Digitization Software for Large-Scale and Intangible Cultural Assets." This work was performed while Mahdi Ammar was an intern at The University of Tokyo (2008.4–7). The internship for Mahdi Ammar was supported in part by the Ministry of Higher Education and Scientific Research in Tunisia. The authors thank Joan Knapp for proofreading and editing this manuscript. They also thank anonymous reviewers for their careful reviews of the paper.

References

1) Hegedüs, R., Åkesson, S. and Horváth, G.: Polarization patterns of thick clouds: Overcast skies have distribution of the angle of polarization similar to that of clear skies, *J. Opt. Soc. Am. A*, Vol.24, No.8, pp.2347–2356 (2007).
2) Pomozi, I., Horváth, G. and Wehner, R.: How the clear-sky angle of polarization pattern continues underneath clouds: Full-sky measurements and implications for animal orientation, *The Journal of Experimental Biology*, Vol.204, pp.2933–2944 (2001).
3) Gál, J., Horváth, G., Meyer-Rochow, V.B. and Wehner, R.: Polarization patterns of the summer sky and its neutral points measured by full-sky imaging polarimetry in Finnish Lapland north of the Arctic Circle, *Proc. R. Soc. Lond. A*, Vol.457, pp.1385–1399 (2001).
4) Voss, K.J. and Liu, Y.: Polarized radiance distribution measurements of sky light. I. System description and characterization, *Applied Optics*, Vol.36, No.24, pp.6083–6094 (Aug. 1997).
5) Horváth, G., Bernáth, B., Suhai, B. and Barta, A.: First observation of the fourth neutral polarization point in the atmosphere, *J. Opt. Soc. Am. A*, Vol.19, No.10, pp.2085–2099 (2002).
6) Suhai, B. and Horváth, G.: How well does the Rayleigh model describe the E-vector distribution of sky light in clear and cloudy conditions? A full-sky polarimetric study, *J. Opt. Soc. Am. A*, Vol.21, No.9, pp.1669–1676 (2004).
7) Rossel, S. and Wehner, R.: The bee's map of the e-vector pattern in the sky, *Proc. Natl. Acad. Sci. USA*, Vol.79, pp.4451–4455 (July 1982).
8) Berry, M.V., Dennis, M.R. and Lee Jr., R.L.: Polarization singularities in the clear sky, *New Journal of Physics*, Vol.6, No.162 (2004).
9) Sabbah, S., Barta, A., Gál, J., Horváth, G. and Shashar, N.: Experimental and theoretical study of sky light polarization transmitted through Snell's window of a flat water surface, *J. Opt. Soc. Am. A*, Vol.23, No.8, pp.1978–1988 (2006).
10) Hannay, J.H.: Polarization of sky light from a canopy atmosphere, *New Journal of Physics*, Vol.6, No.197 (2004).
11) Goldstein, D.H.: *Polarized light*, p.680, Marcel Dekker Inc. (2003).
12) Chandrasekhar, S.: *Radiative Transfer*, p.393, Dover Publications, Inc. (1960).
13) Wehner, R.: Polarization vision — A uniform sensory capacity?, *The Journal of*

Experimental Biology, Vol.204, pp.2589–2596 (2001).

Appendix

A.1 Rayleigh Scattering

A.1.1 Degree of Polarization

In this appendix, we give an overview of the derivation of degree of polarization. The difference from previous authors [2),9)] is that we prove that the observed brightness is independent of the camera response function and the transmittance of the polarization filter. We consider observing the radiated or scattered light at a distance r from the origin along a line that makes an angle $\gamma_{\rm k}$ with the k-axis (Fig. 3 (a)). According to the previous literature [12)], the scattered light intensity $I_{\rm s}$ will be:

$$I_{\rm sk} = \frac{K}{\lambda^4}\sin^2\gamma_{\rm k}, \tag{12}$$

where

$$K = \alpha_p^2 I_0 \frac{16\pi^2}{r^2}, \tag{13}$$

$$I_0 = <E_0^2\cos^2\frac{2\pi ct}{\lambda}>, \tag{14}$$

where $<>$ represents time average. E_0 is the amplitude of the electric field, c is the speed of light, t is time, and λ is the wavelength of light. If the particle at the origin in Fig. 3 is polarizable, the incident electric field will induce a dipole moment in that particle. The magnitude of the dipole moment is proportional to the field. The proportionality constant is called the polarizability $\alpha_{\rm p}$.

The above results are for incident light polarized in the k direction. The sunlight, however, is unpolarized light. Suppose that the light moves along i-axis, and the scattering occurred in (i,j)-plane, as is shown in Fig. 3 (a). Let us denote the angle between the scattering direction and i, j, and k axes as $\gamma_{\rm i}$, $\gamma_{\rm j}$, and $\gamma_{\rm k}$, respectively.

$$I_{\max} = \frac{1}{2}I_{\rm sk}, \tag{15}$$

$$I_{\min} = \frac{1}{2}I_{\rm sj}, \tag{16}$$

$$I_{\rm polarized} = I_{\max} - I_{\min}, \tag{17}$$

$$I_{\rm total} = I_{\max} + I_{\min}, \tag{18}$$

$$d = \frac{I_{\rm polarized}}{I_{\rm total}}, \tag{19}$$

where d represents the degree of polarization.

In Fig. 3, $\gamma_{\rm k} = 90°$. Due to the definition, we have $\cos^2\gamma_{\rm i}+\cos^2\gamma_{\rm j}+\cos^2\gamma_{\rm k} = 1$. Therefore, we have:

$$\sin^2\gamma_{\rm k} - \sin^2\gamma_{\rm j} = 1 - \cos^2\gamma_{\rm i}, \tag{20}$$

$$\sin^2\gamma_{\rm k} + \sin^2\gamma_{\rm j} = 1 + \cos^2\gamma_{\rm i}. \tag{21}$$

If we observe the light shown in Eqs. (15) and (16), the brightness detected by camera is affected by the camera response function $C(\lambda)$ and the transmittance ratio of the polarization filter $F(\lambda)$.

$$I_{\max} = \int_0^\infty \frac{1}{2}C(\lambda)F(\lambda)\frac{K(\lambda)}{\lambda^4}\sin^2\gamma_{\rm k}d\lambda, \tag{22}$$

$$I_{\min} = \int_0^\infty \frac{1}{2}C(\lambda)F(\lambda)\frac{K(\lambda)}{\lambda^4}\sin^2\gamma_{\rm j}d\lambda. \tag{23}$$

From Eqs. (22), (23), (17), (18), (20), and (21), we have:

$$I_{\rm polarized} = \frac{1}{2}\left(1-\cos^2\gamma_{\rm i}\right)\left(\int_0^\infty C(\lambda)F(\lambda)\frac{K(\lambda)}{\lambda^4}d\lambda\right), \tag{24}$$

$$I_{\rm total} = \frac{1}{2}\left(1+\cos^2\gamma_{\rm i}\right)\left(\int_0^\infty C(\lambda)F(\lambda)\frac{K(\lambda)}{\lambda^4}d\lambda\right). \tag{25}$$

From Eqs. (24), (25), (19), and redefining the scattering angle $\gamma = \gamma_{\rm i}$, we have:

$$d = \frac{1-\cos^2\gamma}{1+\cos^2\gamma}. \tag{26}$$

If the physical phenomena strictly obey Rayleigh's theory, the degree of polarization is not affected by the RGB channels of the camera; however, this is not always true in the actual sky since it differs slightly from the ideal Rayleigh sky, and in addition, the polarizability of the actual polarization filter depends slightly on the wavelength.

A.1.2 Angle of Polarization

In this appendix, we give an overview of the derivation of angle of polarization. Unlike the authors of previous papers [2),9)], we will not skip the detailed derivation

since it is useful for understanding sky polarization. Figure 5 represents the Rayleigh sky polarization pattern. γ is the angular distance between the observed celestial point and the sun (Fig. 4):

$$\begin{aligned}\cos\gamma = \mathbf{OM}\cdot\mathbf{OS} &= \begin{bmatrix}\sin\theta\cos\varphi\\ \sin\theta\sin\varphi\\ \cos\theta\end{bmatrix}\cdot\begin{bmatrix}\sin\theta_{\mathrm{s}}\cos\varphi_{\mathrm{s}}\\ \sin\theta_{\mathrm{s}}\sin\varphi_{\mathrm{s}}\\ \cos\theta_{\mathrm{s}}\end{bmatrix}\\ &= \sin\theta\sin\theta_{\mathrm{s}}\left(\cos\varphi\cos\varphi_{\mathrm{s}}+\sin\varphi\sin\varphi_{\mathrm{s}}\right)+\cos\theta\cos\theta_{\mathrm{s}}\\ &= \sin\theta\sin\theta_{\mathrm{s}}\cos\psi+\cos\theta\cos\theta_{\mathrm{s}},\end{aligned} \tag{27}$$

where

$$\psi = \varphi - \varphi_{\mathrm{s}}. \tag{28}$$

γ is constant for all the points of the circle C_γ. Let m be the arc length (or natural parameter) of the regular parametric curve $C_\gamma(m)$. Therefore:

$$\begin{aligned}&\frac{d(\cos\gamma)}{dm} = 0\\ \Leftrightarrow\ &\frac{d\theta}{dm}\left(\cos\theta\sin\theta_{\mathrm{s}}\cos\psi-\sin\theta\cos\theta_{\mathrm{s}}\right)=\frac{d\varphi}{dm}\left(\sin\theta\sin\theta_{\mathrm{s}}\sin\psi\right)\\ \Leftrightarrow\ &\frac{d\varphi}{d\theta}=\frac{d\varphi}{dm}\Big/\frac{d\theta}{dm}=\frac{\cos\theta\sin\theta_{\mathrm{s}}\cos\psi-\sin\theta\cos\theta_{\mathrm{s}}}{\sin\theta\sin\theta_{\mathrm{s}}\sin\psi}.\end{aligned} \tag{29}$$

The angle α shown in Fig. 2 (b) is defined as an angle between the E-vector direction and θ-axis in the local coordinate system formed by θ-axis and φ-axis. According to this local polar coordinate system, the following equation holds:

$$\frac{d\varphi}{d\theta} = \tan\alpha. \tag{30}$$

From Eqs. (29) and (30), we deduce Eq. (2).

(Received March 2, 2009)
(Accepted October 9, 2009)
(Released December 14, 2009)

(Communicated by *Yasuyuki Matsushita*)

Daisuke Miyazaki received a B.S. degree in science, an M.S. degree in information science and technology, and a Ph.D. degree in information science and technology from the University of Tokyo in 2000, 2002 and 2005. He is a lecturer at Hiroshima City University, Japan. After working at the University of Tokyo for two and a half years, the Microsoft Research Asia for a half year, and the University of Tokyo again for a half year, he joined Hiroshima City University. He is an Editorial Advisory Board of The Open Artificial Intelligence Journal. He received the Best Overall Paper Award from VSMM in 2000. His research interests include computer vision and computer graphics. He is a member of ACM and IEEE.

Mahdi Ammar received a B.S. degree in physics and chemistry from Ecole Supérieure de Physique et de Chimie Industrielles (ESPCI) in 2008 and an M.S. degree in optics from Institut d'Optique Graduate School in 2009. His research interests include polarization and microfluidics.

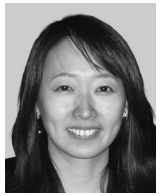

Rei Kawakami received her B.E. and M.E. degrees from the University of Tokyo in 2003 and 2005, respectively. She received her Ph.D. degree in information science and technology at the University of Tokyo in 2008. She is now a project research associate in the Institute of Industrail Science, the University of Tokyo. Her research interests are in color constancy, spectral analysis and physics-based vision. She is a member of IEEE.

Katsushi Ikeuchi received a B.Eng. degree in mechanical engineering from Kyoto University, Kyoto, Japan, in 1973, and a Ph.D. degree in information engineering from the University of Tokyo, Tokyo, Japan, in 1978. He is a professor at the Interfaculty Initiative in Information Studies, the University of Tokyo, Tokyo, Japan. After working at the AI Laboratory at the Massachusetts Institute of Technology for three years, the Electrotechnical Laboratory for five years, and the School of Computer Science at Carnegie Mellon University for 10 years, he joined the University of Tokyo in 1996. He was selected as a distinguished lecturer of the IEEE Signal Processing Society for the period of 2000–2001, and a distinguished lecturer of the IEEE Computer Society for the period of 2004–2006. He has received several awards, including the David Marr Prize in ICCV 1990, IEEE R&A K-S Fu Memorial Best Transaction Paper Award in 1998, and best paper awards in CVPR 1991, VSMM 2000, and VSMM 2004. In addition, in 1992, his paper, "Numerical Shape from Shading and Occluding Boundaries," was selected as one of the most influential papers to have appeared in the Artificial Intelligence Journal within the past 10 years. He is a fellow of the IEEE.